Comprehensive analysis of time-domain overlapping gravitational wave transients: A Lensing Study

Nishkal Rao ⓘ,[1, 2, *] Anuj Mishra ⓘ,[3, 2, †] Apratim Ganguly ⓘ,[2, ‡] and Anupreeta More ⓘ[2, 4, §]

[1] *Department of Physics, Indian Institute of Science Education and Research, Pashan, Pune - 411 008, India*
[2] *Inter-University Centre for Astronomy and Astrophysics (IUCAA),*
Post Bag 4, Ganeshkhind, Pune 411 007, India
[3] *International Centre for Theoretical Sciences, Tata Institute of Fundamental Research, Bangalore 560089, India*
[4] *Kavli IPMU (WPI), UTIAS, The University of Tokyo, Kashiwa, Chiba 277-8583, Japan*

Next-generation gravitational-wave (GW) detectors will produce a high rate of temporally overlapping signals from unrelated compact binary coalescences. Such overlaps can bias parameter estimation (PE) and mimic signatures of other physical effects, such as gravitational lensing. In this work, we investigate how overlapping signals can be degenerate with gravitational lensing by focusing on two scenarios: Type-II strong lensing and microlensing by an isolated point-mass lens. We simulate quasicircular binary black-hole pairs with chirp-mass ratios $\mathscr{M}_B/\mathscr{M}_A \in \{0.5, 1, 2\}$, signal-to-noise ratio (SNR) ratios $\mathrm{SNR_B}/\mathrm{SNR_A} \in \{0.5, 1\}$, and coalescence-time offsets $\Delta t_c \in [-0.1, 0.1]$ s, and extend to a population analysis. Bayesian PE and fitting-factor studies show that the Type-II lensing hypothesis is favored over the unlensed quasicircular hypothesis ($\log_{10} \mathscr{B}_U^L > 1$) only in a small region of the overlapping parameter space with $\mathscr{M}_B/\mathscr{M}_A \gtrsim 1$ and $|\Delta t_c| \leq 0.03$ s, with the inferred Morse index clustering near $n_j \simeq 0.5$, indicative of Type-II lensing, for the cumulative study. Meanwhile, false evidence for microlensing signatures can arise because, to a reasonable approximation, the model produces two superimposed images whose time delay can closely match $|\Delta t_c|$. The microlensing hypothesis is maximally favored ($\log_{10} \mathscr{B}_U^L \gg 1$) for $\mathscr{M}_B/\mathscr{M}_A \gtrsim 1$ and equal SNRs, increasing with $|\Delta t_c|$. The inferred redshifted lens masses lie in the range $M_L^z \sim 10^2$–10^5 $M_\odot$ with impact parameters $y \sim 0.1$–3. Overall, the inferred Bayes factor depends on relative chirp-mass ratios, relative loudness, difference in coalescence times, and also the absolute SNRs of the overlapping signals. Cumulatively, our results indicate that overlapping black-hole binaries with nearly equal chirp masses and comparable loudness are likely to be falsely identified as lensed. Such misidentifications are expected to become more common as detector sensitivities improve. While our study focuses on ground-based detectors using appropriate detectability thresholds, the findings naturally extend to next-generation GW observatories.

I. INTRODUCTION

The detection of gravitational waves from merging compact binary coalescences (CBCs) has become routine with the Advanced LIGO [1] and Advanced Virgo [2] detectors, culminating in 90 events in the third Gravitational-wave Transient Catalog (GWTC-3) [3]. The detection rate has increased rapidly, from around twice a month to about twice a week during the current fourth observational run (O4) [4] of the detectors, where the number of significant detection candidates has more than doubled the GWTC-3 events by the end of the second part of O4. With planned upgrades to second-generation detectors, including KAGRA [5–8], and the addition of LIGO-India [9–11], the field is assured for a surge in observed events. Future detectors with enhanced low-frequency sensitivity, such as Einstein Telescope (ET) [12, 13] and Cosmic Explorer (CE) [14–16], will enable detection of longer inspiral cycles [17–19]. This will increase the probability that two or more GW signals will temporally overlap in the detector band [20–29].

Table I summarises prior investigations of overlapping CBC signals, including their impact on search efficiency, PE biases, and tests of general relativity (GR). We further highlight the degree of overlap in each study by reporting the difference in coalescence times, Δt_c, between the lower- and the higher-SNR signal.

These studies show that parameter biases depend on signal-to-noise ratios (SNRs), chirp masses, and Δt_c, with the largest biases typically arising for small time separations and similar binary black hole (BBH) intrinsic parameters [21–25]. For instance, the inferred chirp masses can be biased by 20–30% in the worst cases, especially for small merger time differences [23, 25]. The Fisher matrix analyses in Ref. [22] and Ref. [25] conclude that biases are typically 10%–30% of the statistical errors for closely timed BBHs, and are more pronounced than for binary neutron star (BNS) mergers. Mitigation strategies such as hierarchical subtraction and joint parameter estimation [26, 37] have proven more reliable, though the latter is computationally expensive over the full 30-dimensional parameter space of two BBHs. More recently, Ref. [38] have proposed using prior-informed Fisher matrices, overlap of time-frequency tracks to predict the magnitude of biases, as a systematic choice between hierarchical subtraction and joint parameter estimation depending on the expected bias and computational constraints.

Search studies demonstrate that matched-filter

Type	Ref.	Remarks	Concerned Regime
PE	[23]	Studied biases from differences in merger times, SNRs, chirp masses, and initial phases.	$\lvert\Delta t_{\rm c}\rvert < 0.1$ s
PE	[21]	Analyzed overlaps of BBH and BNS signals, studying effects of mass, and SNRs.	$\Delta t_{\rm c} = 0, \pm 2$ s
PE	[24]	Examined metrics for PE biases on individually resolved sources from the presence of confusion noise and waveform inaccuracies.	$\lvert\Delta t_{\rm c}\rvert < 1$ s
PE	[25]	Investigated statistical impacts of overlapping GWs using Fisher matrix analysis.	$\lvert\Delta t_{\rm c}\rvert < 0.1$ s
Search	[30]	Evaluated search efficiency for overlapping signals with modeled and unmodeled pipelines.	$\Delta t_{\rm c} < 1$ s
PE	[22]	Explored overlaps of non-spinning binaries, varying coalescence times, phases, and SNRs.	$\Delta t_{\rm c} < 0.5$ s
PE	[26]	Implemented joint PE and hierarchical subtraction for high-mass, medium-SNR events.	$\lvert\Delta t_{\rm c}\rvert = 1$ s
TGR	[31]	Investigated impacts of overlapping signals and waveform inaccuracies on tests of GR.	$\lvert\Delta t_{\rm c}\rvert < 4$ s
PE	[32]	Combined Fisher matrix and Bayesian analysis to compute biases in inferred posteriors.	$\lvert\Delta t_{\rm c}\rvert < 0.1$ s
PE	[33]	Applied machine learning to PE of overlapped BBH systems.	$\lvert\Delta t_{\rm c}\rvert \leq 0.05$ s
PE	[34]	Performed sequential simulation-based joint PE for efficient inference.	$\Delta t_{\rm c} = 0.05, 0.2, 0.5$ s
TGR	[35]	Studied overlapping impacts on post-Newtonian coefficients in GR tests.	$\Delta t_{\rm c} \in 0.1 - \mathcal{O}(10)$ s
PE	[36]	Investigated the time-frequency overlap and the impact on PE studies over BNS populations and binary parameters.	$\lvert\Delta t_{\rm c}\rvert < 0.1$ s

Table I. Overview of previous works on overlapping GWs (listed chronologically) focused on parameter estimation (PE), searches, or biases in tests of GR. The final column highlights the range of coalescence time differences between the lower and the higher SNR signals, $\Delta t_{\rm c}$, indicating regimes of interest for studying overlapping signals.

searches [30] and burst pipelines [39–41] remain effective for $\lvert\Delta t_{\rm c}\rvert \geq 1$ s, while BNSs overlap analyses [36] found that 91% of the overlaps occur at low frequencies ($\lesssim 5$ Hz) where the inspiral evolution is slow. Overlapping signals have also been shown to bias tests of GR, particularly in post-Newtonian coefficients [31, 35, 42].

While these studies explored the impact of overlapping signals on searches and PE, none have examined the potential for degeneracies with other atypical physical effects, such as gravitational lensing and orbital eccentricity. Such a degeneracy could arise because overlapping CBC signals can produce amplitude and phase modulations resembling the frequency-dependent magnifications of *microlensing*, the phase shifts of certain *strongly lensed* images, and the modulation due to non-zero eccentricities. Fig. 1 illustrates two examples of overlapping BBH signals with different and similar SNRs, showing how their superposition can lead to complex waveform morphologies.

This work investigates, for the first time, the degeneracy between overlapping CBC signals and gravitationally lensed signals in the context of ground-based detectors. By overlapping, we refer to two distinct (quasicircular, unlensed) BBH signals whose coalescence times differ by $\lvert\Delta t_{\rm c}\rvert < 0.1$ s, with varied chirp mass ratios, SNRs, and temporal overlap.

We focus on two lensing scenarios: (i) *Microlensing* in the wave-optics regime, where the GW wavelength is comparable to the Schwarzschild radius of an intervening compact lens, such as a stellar-mass black hole [47, 48], and (ii) *Type-II Strongly Lensed images*, produced by galaxy- or cluster-scale lenses and differing from type-

I images by a relative phase shift of $-\pi/2$ [49]. Fig. 2 compares an injected overlapping GW signal to its best-fit lensed counterparts, illustrating how these models can reproduce the overlap-induced modulations.

Since performing joint PE for overlapping signals is computationally far more expensive than analyzing them under the microlensing or type-II lensing hypotheses, we adopt an approach in which we only *inject* overlapping signals and use lensing as the inference model for computing evidences (i.e., marginalized likelihoods). By *injection*, we refer to simulated observations of two overlapping GW signals in the detectors, termed as SINGLES$_{\rm A}$ and SINGLES$_{\rm B}$, with SINGLES$_{\rm A}$ having the higher SNR. Specifically, we consider only zero-noise injections to isolate the effects arising purely from overlapping signals; noise-systematic effects are left to future work. Using the three-detector network of Hanford, Livingston, and Virgo at A+ design sensitivity, we compare and evaluate the extent to which the two lensing models can mimic overlapping GW signals. We use fitting factor (FF) calculations and PE techniques to analyze the overlapping signals and identify regions in their parameter space, characterized by chirp mass ratios, SNR ratios, and temporal overlap, that can potentially be misinterpreted as lensing effects.

The paper is organized as follows: Sec. II outlines the basics of gravitational lensing, Sec. III describes the methods for analyzing overlapping signals, Sec. IV explains the analysis setup, Sec. V presents the results, and Sec. VI concludes with an outlook.
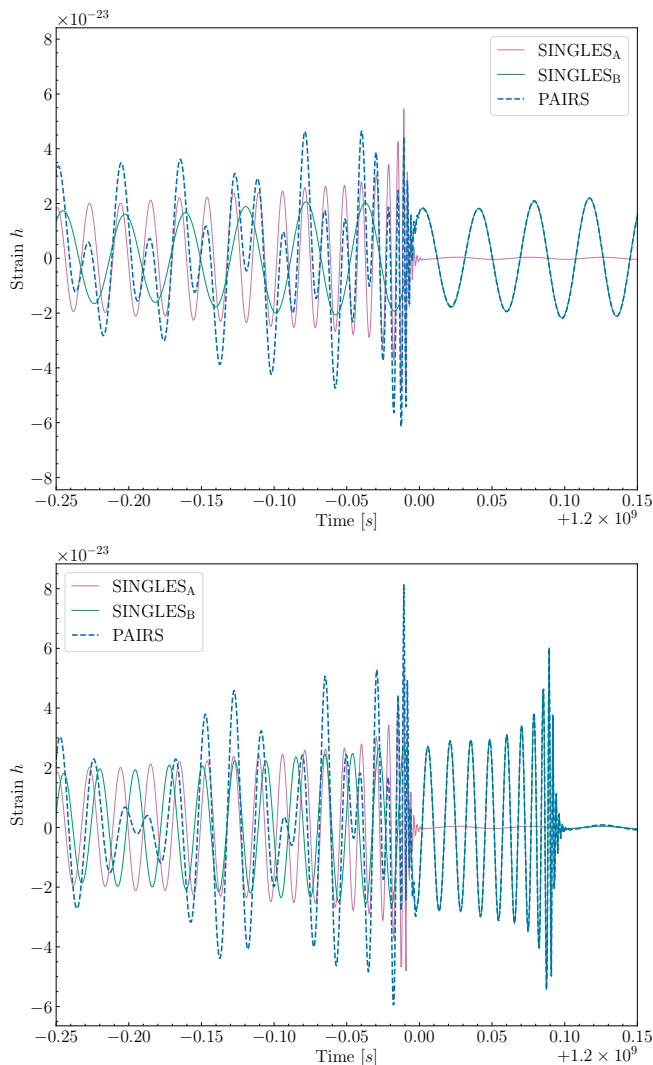
Figure 1. Representation of two BBH signals (SINGLES$_A$ and SINGLES$_B$) producing an overlapping strain (termed PAIRS). *Top:* Different SNRs: The primary signal (termed SINGLES$_A$, with SNR = 30) resembles the GW150914-like merger [43–45], and the secondary signal (termed SINGLES$_B$, with SNR = 15) resembles the GW170814-like merger [45, 46], which coalesces $\Delta t_c = 0.15$ s after the merger of the primary signal. The louder signal dominates until its merger-ringdown phase, after which the quieter one becomes visible. *Bottom:* Similar SNRs: both signals resemble the GW150914-like merger, producing a more strongly modulated waveform with no single signal dominating throughout, with $\Delta t_c = 0.1$ s.

II. GRAVITATIONAL LENSING

Gravitational lensing of a GW signal occurs when it passes through the gravitational potential of an intervening astrophysical object, such as a galaxy, galaxy cluster, star, or black hole. The effect depends on the mass distribution of the lens and the source-lens-observer alignment, but in all cases, the lensed waveform can be expressed as,

$$\tilde{h}_L(f; \lambda) = \tilde{h}(f; \lambda)\, F(f, \Theta)\,, \qquad (1)$$

where $\tilde{h}(f; \lambda)$ is the unlensed waveform in the frequency domain, λ denotes the intrinsic and extrinsic binary source parameters (masses, spins, sky location, luminosity distance, inclination, polarisation, coalescence time, and phase), and Θ describes the lens parameters. For an isolated point-mass lens, $\Theta = \{M_L^z, y\}$, where $M_L^z \equiv M_L(1 + z_L)$ is the redshifted lens mass with z_L being the redshift of the lens, and y is the source–lens angular separation in units of the Einstein radius.

The complex, frequency-dependent amplification factor $F(f, \Theta)$ encodes the lensing effect. For a given lens profile, it can be computed using the diffraction integral [48],

$$F(w, y) = \frac{w}{2\pi i} \int d^2x \, \exp[iwT(x, y)]\,, \qquad (2)$$

where x and y are the image- and source-plane coordinates in units of the lens scale ξ_0 (typically the Einstein radius), and $T(x, y)$ is the dimensionless time-delay function. The dimensionless frequency is

$$w = \frac{D_{OS}}{D_{OL} D_{LS}} \xi_0^2 (1 + z_L) 2\pi f\,, \qquad (3)$$

with D_{XY} the angular-diameter distances between observer (O), lens (L), and source (S). The value of w determines the relevant lensing regime.

Strong lensing (geometric optics): When $w \gg 1$ for the frequencies of interest, only stationary points of $T(x, y)$ contribute significantly to Eq. (2), and the amplification factor for image j reduces to [49, 50],

$$F_j(f) = |\mu_j|^{1/2} \exp[2\pi i f t_j - i\pi n_j \, \text{sgn}(f)]\,. \qquad (4)$$

Here μ_j is the magnification, t_j is the arrival-time delay due to path length and Shapiro delay, and n_j is the Morse index determined by the image type: $n_j = 0$ (Type-I, minima), $n_j = 1/2$ (Type-II, saddle points), or $n_j = 1$ (Type-III, maxima), corresponding to phase shifts of 0, $-\pi/2$, and $-\pi$, respectively. In this work, we model *Type-II* images following previous studies [51, 52], in which the $-\pi/2$ phase shift imprints frequency-dependent distortions across the waveform.

Microlensing (wave optics): When $w \sim \mathcal{O}(1)$, the GW wavelength is comparable to the Schwarzschild radius of the lens, and the geometric-optics approximation fails. The full diffraction integral in Eq. (2) must be evaluated. For an isolated point-mass lens, $F(f; M_L^z, y)$ admits an analytical expression: a complex, frequency-dependent magnification that produces characteristic oscillatory modulations in the amplitude and phase of $\tilde{h}_L(f; \lambda)$ [47, 48].

Using the methods outlined in Ref. [53] and Ref. [54], we generate microlensed signals with an isolated point lens model [55]. This simple yet effective lensing profile enables detailed parameter estimation and mismatch analysis for overlapping signals. Previous studies [52, 56] have extensively employed this model in microlensing searches due to its computational efficiency.

This study uses Type-II strong-lensing and point-mass microlensing models as inference templates for overlapping GW signals. Both models can produce characteristic
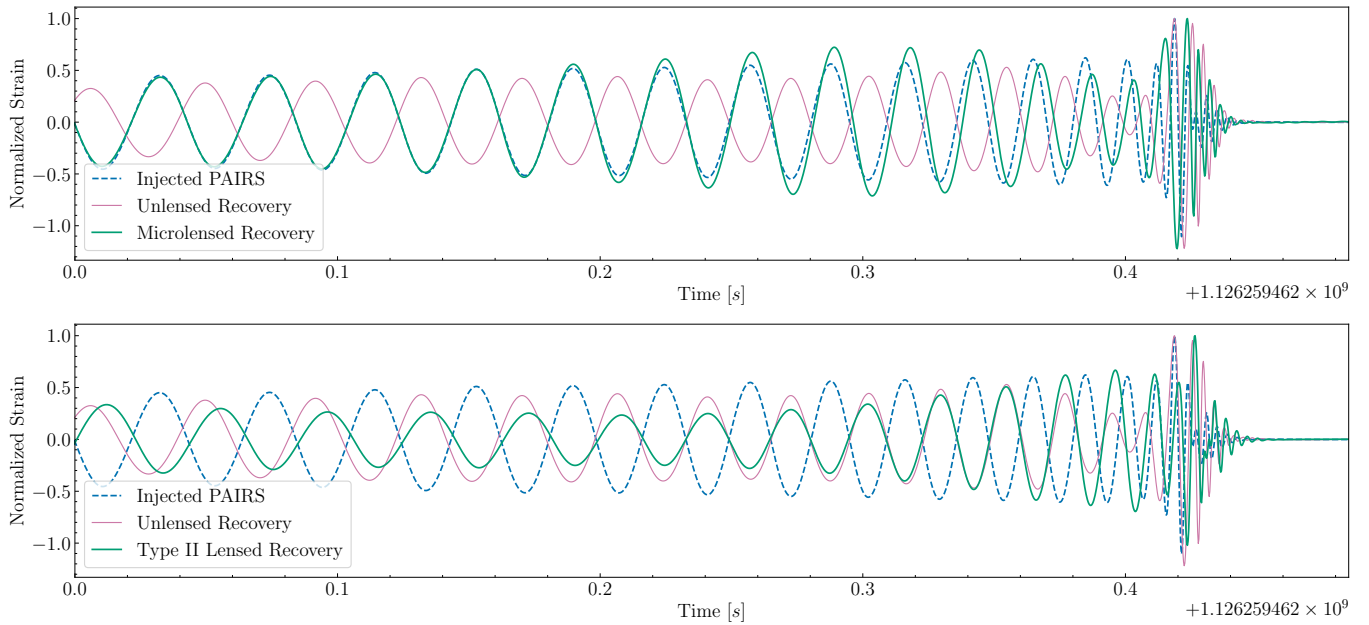
Figure 2. Illustration of waveform morphology similarities between an overlapping signal and its best-fit lensed counterparts. The injected overlapping waveform at the detector and the corresponding best-fit normalized lensed waveforms obtained from the inferred values from PE are shown. The normalized strain is defined as the ratio of strain h to the maximum amplitude $|h|$. *Top:* Contains an injected overlapping waveform (termed PAIRS) from a combination of two GW signals (SINGLES$_A$ and SINGLES$_B$) with relative parameters of chirp mass ratio, $\mathcal{M}_B/\mathcal{M}_A = 0.5$, SNR ratio, SNR$_B$/SNR$_A = 1$, and coalescence time difference, $\Delta t_c = 0.02$ s, and its corresponding inferred Unlensed and Microlensed waveforms. *Bottom:* Contains the same overlapping strain as above, but with the inferred Type-II lensed waveform. Notably, the microlensed model provides a visibly better match to the modulated structure of the overlapping signal, especially near the merger phase.

amplitude and phase modulations; a $-\pi/2$ phase shift for Type-II images in the geometric-optics limit, and oscillatory patterns in the wave-optics regime for microlensing. These patterns may be similar to overlapping signatures, creating a potential for degeneracy. These models have been employed in GW lensing studies [51–54, 56–60] and are therefore well-suited for the PE and FF analyses presented in this study. However, it is worth noting that model-independent approaches for detecting lensed signals also exist [61, 62], although they are not utilized in this study.

III.   DESCRIPTIONS OF METHODS

A.   Parameter Estimation Techniques

This work uses Bayesian parameter estimation to test whether overlapping GW signals are better inferred with lensed or unlensed templates and to quantify the resulting parameter biases. Given data d and hypothesis $\mathcal{H}$, the posterior for parameters θ is

$$p(\theta|d, \mathcal{H}) = \frac{\mathcal{L}(d|\theta, \mathcal{H})\,\pi(\theta|\mathcal{H})}{\mathcal{Z}(d|\mathcal{H})}, \qquad (5)$$

where $\pi(\theta|\mathcal{H})$ is the prior, $\mathcal{L}(d|\theta, \mathcal{H})$ is the likelihood, and $\mathcal{Z}(d|\mathcal{H})$ is the evidence, which is the marginalised likelihood.

Assuming stationary Gaussian noise, the likelihood is

$$\mathcal{L}(d|\theta, \mathcal{H}) \propto \exp\left[-\frac{1}{2}\langle d - h(\theta)|d - h(\theta)\rangle\right], \qquad (6)$$

with the noise-weighted inner product

$$\langle a|b\rangle = 4\,\mathrm{Re}\int_{f_{\min}}^{f_{\max}} \frac{\tilde{a}(f)\,\tilde{b}^*(f)}{S_n(f)}\,df\,. \qquad (7)$$

Here, $S_n(f)$ is the power spectral density (PSD) of the detector, and $f_{\min}$ and $f_{\max}$ are the analysis frequency bounds[1]. We use the target PSDs for the O4 observing run of the Advanced LIGO and Virgo detectors[2] [63].

The evidence enables model selection under the Bayesian framework. Comparing a lensed hypothesis ($\mathcal{H}_L$) with an unlensed one ($\mathcal{H}_U$) yields the Bayes factor

$$\log_{10}\mathscr{B}_U^L = \log_{10}\mathcal{Z}_L - \log_{10}\mathcal{Z}_U\,. \qquad (8)$$

Since lensing effects are applied on top of the standard quasicircular unlensed waveform, π_U is a subset of π_L. The PE results in Sec. V quantify both the inference accuracy and the statistical preference between models.

----

[1] Typically, $f_{\min}$ corresponds to the lowest frequency where the detector noise can be approximated as stationary, while $f_{\max}$ denotes the Nyquist frequency.

[2] For the LIGO detectors, we use the PSD provided here, and for Virgo, we use the PSD available here.

Parameter	Population Model	PE Priors
BBH Parameters		
$\mathscr{M}$: Chirp Mass	–	$\mathcal{U}(15, 50)$ M$_\odot$
q: Mass ratio	–	$\mathcal{U}(0.05, 1)$
m_1, m_2: Component Masses	POWERLAW + PEAK [64]: [5, 100] M$_\odot$	Constraint: [3.5, 130] M$_\odot$
z: Redshift	POWERLAW [65]	–
d_L: Luminosity distance	Interpreted from z	POWERLAW$_{\alpha=2}$(50, 5000) Mpc
$a_{1/2}$: Spin amplitude 1/2	Beta distribution (i.i.d[a])	$\mathcal{U}(0, 1)$
$\theta_{1/2}$: Tilt angle 1/2	Truncated normal in cosine (i.i.d)	Uniform in $\sin\theta$
ϕ_{12}: Spin vector azimuthal angle	$\mathcal{U}(0, 2\pi)$	$\mathcal{U}(0, 2\pi)$
ι: Inclination angle	$\mathcal{U}(0, \pi)$	$\mathcal{U}(0, \pi)$
ψ: Wave polarisation	$\mathcal{U}(0, \pi)$	$\mathcal{U}(0, \pi)$
Φ_c: Phase of coalescence	$\mathcal{U}(0, 2\pi)$	$\mathcal{U}(0, 2\pi)$
α: Right ascension	$\mathcal{U}(0, 2\pi)$	$\mathcal{U}(0, 2\pi)$
δ: Declination	Uniform in $\cos\delta$	Uniform in $\cos\delta$
Type-II Strong Lensing Parameter		
n_j: Morse Phase	–	Fixed: $\delta(n_j - 0.5)$ Varying: $\mathcal{U}(0, 1)$
Microlensing Parameters		
y: Impact Parameter	–	POWERLAW$_{\alpha=2}$(0.01, 5)
M_L^z: Redshifted Lens Mass	–	Log-Uniform in $[0.1, 10^5]$ M$_\odot$

[a] i.i.d refers to independent and identically distributed [66].

Table II. Overview of the functions used to generate the BBH populations for SINGLES$_A$ and SINGLES$_B$, along with the priors employed in parameter estimation. Additional priors specific to microlensed and Type-II analyses are also included.

B. Fitting Factor Analysis

To complement PE inferences, which are computationally expensive, we use fitting factor studies [67, 68] as fast diagnostics of waveform degeneracy between overlapping signals and lensed templates.

The overlap between two waveforms is

$$\mathcal{O}[h_1, h_2] = \frac{\langle h_1 | h_2 \rangle}{\sqrt{\langle h_1 | h_1 \rangle \langle h_2 | h_2 \rangle}}, \qquad (9)$$

and the match $\mathcal{M}[h_1, h_2]$ is the maximum overlap over coalescence time t_c and phase Φ_c.

The fitting factor is

$$\mathscr{F} = \max_\theta \mathcal{M}[h_s, h_T(\theta)], \qquad (10)$$

where $h_s = \sum_{i \in \{A,B\}} h_i$ is the overlapping GW signal and $h_T(\theta)$ is the template.

Optimization over intrinsic parameters is performed using Differential Evolution (DE), which ensures robustness across parameter space, unlike the Nelder-Mead (NM) method [11, 53, 54, 69–73], which is biased by the initial data. Extrinsic parameters are excluded as they only affect the waveform through an overall amplitude scaling and phase shift.

The fitting factor can be related to the recovered matched-filter SNR [74, 75],

$$\langle \rho(\theta) \rangle = \mathscr{F} \cdot \rho_{opt}, \qquad (11)$$

where $\rho_{opt} = \langle h | h \rangle = \max_\theta \langle \rho(\theta) \rangle$ is the optimal SNR.

In the high-SNR limit, this yields an approximate relation between the FF and the Bayes factor [76], through a Laplace approximation [77],

$$\ln \mathscr{B}_U^L \approx \frac{1}{2} \rho_{opt}^2 \left(\mathscr{F}_L^2 - \mathscr{F}_U^2 \right), \qquad (12)$$

assuming equal noise evidence and neglecting Occam factors. We compute network fitting factors via a quadrature sum across detectors, analogous to the network SNR. High FF values ($\mathscr{F} \gtrsim 1$) correspond to $\sim 90\%$ detection efficiency [76, 78, 79], ensuring minimal SNR loss.

By combining PE and FF analyses, we can assess the parameter space of overlapping signals that is degenerate with lensing.

IV. SETUP OF THE ANALYSES

Our study investigates pairs of overlapping BBH signals, analysed with both Type-II strong-lensing and microlensing waveform models. We generate three injection sets: two with individual, non-overlapping BBHs (SINGLES$_A$ and SINGLES$_B$) and one containing overlapping pairs (PAIRS). Waveforms are generated with the `IMRPhenomXPHM` approximant [80–84] from the `LALSuite` package [85, 86], setting spins to zero unless otherwise stated.

Relative parameter space: We characterise an overlapping pair by the chirp-mass ratio $\mathscr{M}_B / \mathscr{M}_A$, the network-

SNR ratio $\mathrm{SNR_B/SNR_A}$, and the coalescence-time difference $\Delta t_\mathrm{c} = t_\mathrm{c}^\mathrm{B} - t_\mathrm{c}^\mathrm{A}$. These quantities control the combined waveform morphology: $\mathscr{M}$ influences the signal duration, the SNR ratio sets the relative amplitude, and Δt_c governs the degree of overlap [20–27]. Without loss of generality, $\mathrm{SINGLES_A}$ is defined to have the higher SNR, since, if two different signals arrive within 0.1 s window (trigger window considered for searches [75, 87]), they are most likely to be analysed as a single event. In our preliminary analyses and through matched filtering studies [23, 36], we have observed that the parameters of the signal with higher SNR are obtained.

We explore a 3D grid of 60 points: $\mathscr{M}_\mathrm{B}/\mathscr{M}_\mathrm{A} \in \{0.5, 1, 2\}$, $\mathrm{SNR_B/SNR_A} \in \{0.5, 1\}$, and Δt_c logarithmically sampled in $[-0.1, 0.1]\,\mathrm{s}$ (10 samples in the strong-overlap regime). $\mathrm{SINGLES_A}$ parameters are based on GW150914 [43–45] and $\mathrm{SINGLES_B}$ on GW170814 [45, 46], with luminosity distances scaled so that $\mathrm{SINGLES_A}$ has network optimal SNR $\rho_\mathrm{opt} = 30$. The mass ratios of $\mathrm{SINGLES_A}$ and $\mathrm{SINGLES_B}$ are consequently fixed to 0.81 and 0.87, respectively, which are nearly identical.

We further extend the analysis to a BBH population samples of $\mathcal{O}(5000)$ signals, drawn from GWTC-3–like distributions. The BBH waveforms were generated using the `IMRPhenomXPHM` waveform approximant, with the parameter distributions in Table II, sampled with the `gwpopulation` package [88]. A threshold network SNR of 12 ensured the inclusion of detectable signals, with Δt_c logarithmically sampled in $[-0.1, 0.1]$ s.

Detector configuration and noise model: All injections use the HLV network (Advanced LIGO Hanford and Livingston at design sensitivity [1], Advanced Virgo [2]), analyzed under zero-noise conditions to isolate waveform-systematic effects from noise fluctuations.

Analysis pipeline: Bayesian PE is performed on the 60 signals with `BILBY` [89–91] using the `Dynesty` sampler [92]. Table II summarizes the injection distributions and PE priors, including lensing-specific ones. Type-II strong-lensing templates incorporate the Morse index n_j as a $-\pi/2$ phase shift, and further vary the Morse index as a free parameter. Microlensed templates include the frequency-dependent amplification factor computed via the `gwmat` package[3]. For each overlapping pair, analyses are repeated with unlensed templates to assess degeneracies between overlap effects and lensing.

Fitting factors are computed following Eq. (10) using `PyCBC` [93] with a DE optimization algorithm [94, 95]. Intrinsic parameters to be maximized over, cover $\{\mathscr{M}, \eta\}$ for unlensed signals, extended to include $\{n_j\}$ for Type-II and $\{M_\mathrm{L}^z, y\}$ for microlensing. The FF-derived Bayes factor is estimated via Eq. (12) for the extended BBH population.

---

[3] https://git.ligo.org/anuj.mishra/gwmat/

V.   RESULTS AND DISCUSSIONS

We present results for overlapping GW transients using two complementary approaches:(i) Bayesian PE for a discrete set of cases, and (ii) FF studies over a broader BBH population. Both analyses are used to quantify parameter biases and identify regions of degeneracy when overlapping signals are inferred with lensing models.

A.   Parameter Estimation

We first analyze 60 overlapping cases across the relative parameter space of overlapping signals. As mentioned previously in Sec. IV, the SNR of $\mathrm{SINGLES_A}$ is fixed to 30, with $\mathrm{SINGLES_A}$ always being the louder signal.

Unlensed Quasicircular Model: For the null hypothesis of an unlensed quasicircular GW signal, we observe that strong temporal overlap $|\Delta t_\mathrm{c}| < 0.03$ s frequently produces *bimodal* posteriors in the inferred chirp mass, observed in 13 of the 60 cases. In such cases, the inferred chirp mass deviates from the chirp mass of either overlapping signal, and the inferred SNRs are also significantly lower. This suggests that strong overlap can induce degeneracies in the intrinsic mass parameters that the unlensed model cannot resolve.

Fig. 3 summarizes the inferred chirp mass biases and the inferred SNRs for the unlensed runs. Since only $\mathrm{SNR_A}$ is fixed in our injections, the total network SNR varies across the grid, both due to intrinsic changes in the injected signals and also the mismatches between the injections and the unlensed templates. This dependence is important because the Bayes factor scales steeply with SNR (Eq. 11); therefore, the results in Fig. 3 are directly relevant for interpreting the model comparison outcomes discussed later.

The inferred chirp mass for the louder signal ($\mathrm{SINGLES_A}$) is typically accurate to within 20%. In contrast, the weaker signal ($\mathrm{SINGLES_B}$) exhibits significantly larger systematic biases, up to 200% in extreme cases. This asymmetry likely arises because the inferred geocentric time aligns more closely with that of the louder signal, yielding more accurate parameter estimates for $\mathrm{SINGLES_A}$. When the chirp mass ratios and SNRs of the two signals are comparable and the overlap is strong, the bias in the weaker signal's chirp mass ($\mathscr{M}_\mathrm{B}$) becomes severe, and the effective SNR drops significantly. Even in cases with asymmetric chirp mass ratios but equal SNRs, we see gradations in inferences, indicating that the parameter degeneracies depend on both intrinsic and extrinsic factors.

1.   Type-II Lensed Image Model

We next model the same set of overlapping signals with a strongly-lensed template corresponding to a Type-II image. Fig. 4 compares results for two inference settings: a Type-II configuration i) with $n_j = 0.5$ (left), and (ii) a free Morse index $n_j \in [0, 1]$ (middle and right). In both cases,
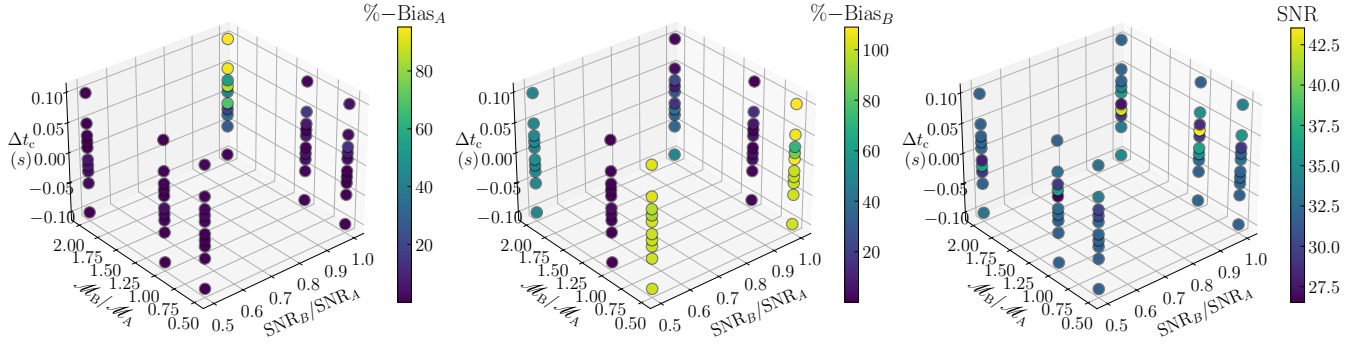
Figure 3. Inferred relative biases in the inferred chirp mass and the recovered SNR from PE on injected overlapping signals, assuming an unlensed quasicircular signal model. The chirp mass bias for each signal is defined as the relative difference between the inferred chirp mass and the mass of the injected signal. Variations in the recovered SNR reflect both the differences in the true injected SNR and the mismatches between the injections and the unlensed templates.
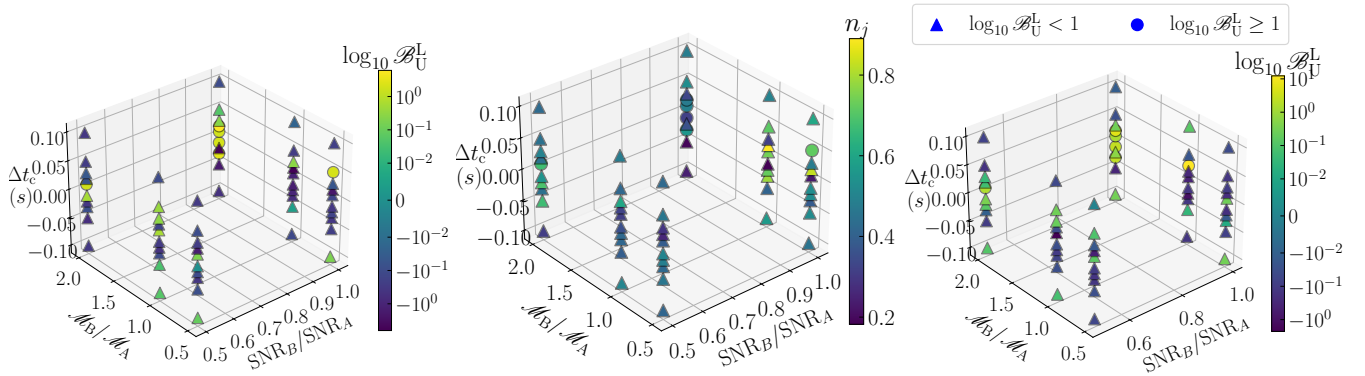

Figure 4. Results of fitting Type-II lensed templates to overlapping signals as a function of chirp mass ratio, SNR ratio, and coalescence time difference. *Left:* Inferred Bayes factors for a Type-II image ($n_j = 0.5$). *Middle and Right:* Results when the Morse phase n_j is a free parameter. Circular markers indicate $\log_{10} \mathscr{B}_{\mathrm{U}}^{\mathrm{L}} \geq 1$, corresponding to strong support for lensing.

strong overlaps ($|\Delta t_c| \lesssim 0.02$ s) yield a mild but noticeable preference for Type-II lensing, indicated by positive values of lensed-to-unlensed Bayes factor, $\log_{10} \mathscr{B}_{\mathrm{U}}^{\mathrm{L}}$. For moderate to large temporal separations ($|\Delta t_c| \gtrsim 0.05$ s), or for strong SNR asymmetries, the preference disappears and the Bayes factors support the unlensed model. Consistent with previous studies [96–99], we adopt $\log_{10} \mathscr{B}_{\mathrm{U}}^{\mathrm{L}} > 1$ (highlighted using circular markers in the relevant plots throughout this paper) as the threshold for strong support of the lensing hypothesis.

Fig. 5 shows that when n_j is allowed to vary, both the maximum likelihood estimate (MLE) value and the median of the 1D marginalized posterior often cluster near 0.5 for overlapping injections[4], which indicates a Type-II

lensed image. Wider time separations ($|\Delta t_c| \gtrsim 0.02$ s) cause the n_j posterior to broaden or shift away from 0.5, reflecting the fact that a single lensed image cannot fit distinct time–frequency features any better than the null hypothesis of a quasicircular unlensed signal. The fact that MLE values, which are independent of the prior volume effects, still peak near 0.5 reinforces that this clustering is a genuine feature of the data in the high-overlap regime.

2. Microlensed Model

We next investigate the ability of the microlensed model to fit overlapping signals. Fig. 6 shows the inferred microlensed parameters (left and middle) and the Bayes factors comparing the microlensed and unlensed hypotheses (right). The maximum support for the microlensing hypothesis occurs when $\mathscr{M}_{\mathrm{B}}/\mathscr{M}_{\mathrm{A}} = 1$ and $\mathrm{SNR}_{\mathrm{B}}/\mathrm{SNR}_{\mathrm{A}} = 1$, and this support increases as $|\Delta t_c|$ moves away from zero, attaining a maximum at

---

[4] Since we use a uniform prior on n_j, the median of a weakly constrained posterior tends to lie near 0.5. To mitigate this prior-induced bias, we also report MLE estimates.
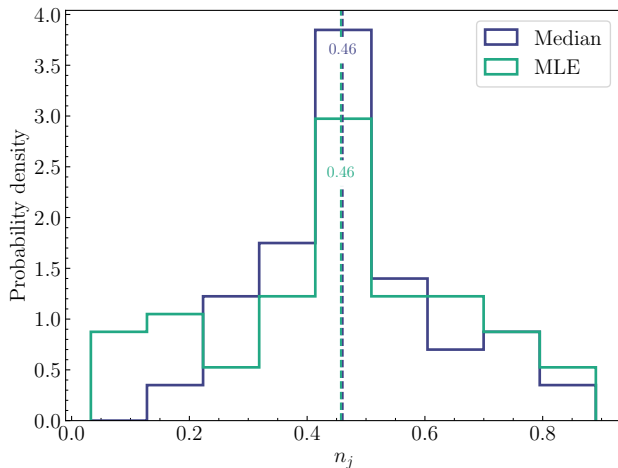
Figure 5. Inferred Morse index n_j densities from parameter estimation under the Type-II lensing hypothesis for all 60 injections. Posterior medians (*purple*) and maximum likelihood estimate, MLE (*green*) values show clustering near $n_j = 0.5$, indicating a preference for a saddle-point (Type-II) image. Dashed lines denote the overall medians across the 60 runs.

$|\Delta t_c| = 0.1$ s. This trend is expected, since in the geometric-optics regime of the microlensed parameter space considered here, a microlensed signal is well approximated as the superposition of two images, with detector-frame chirp masses remaining invariant across lensed images. The rise in Bayes factors with increasing $|\Delta t_c|$ can be understood if the microlens-induced effective time delay becomes comparable to the injected Δt_c.

For $\mathrm{SNR_B/SNR_A} = 1$ and $\mathscr{M}_B/\mathscr{M}_A = 2$, all values of Δt_c showed preference for microlensing. In contrast, for $\mathrm{SNR_B/SNR_A} = \mathscr{M}_B/\mathscr{M}_A = 0.5$ no case preferred microlensing. For the mixed cases $\mathrm{SNR_B/SNR_A} = 0.5$, $\mathscr{M}_B/\mathscr{M}_A = 2$ and $\mathrm{SNR_B/SNR_A} = 1$, $\mathscr{M}_B/\mathscr{M}_A = 0.5$ preference for microlensing was observed only when $\Delta t_c > 0$.

Fig. 7 shows the inferred 2D marginalized joint posteriors for the redshifted lens mass and impact parameter versus coalescence time difference. Only cases with substantial evidence[5] in favor of microlensing ($\log_{10} \mathscr{B}_U^L > 0.5$) are shown for clarity. The inferred redshifted lens masses range from $\sim 10^2$ to 10^5 M$_\odot$, with impact parameters varying between ~ 0.1 and 3. We note that as $|\Delta t_c|$ decreases from 0.1 s to 0.01 s, the inferred $\log_{10} M_L^z$ and y values typically decrease, that is, from higher lens masses and impact parameters, indicative of the geometric optics regime, to lower values where wave optics effects dominate.

---

[5] We use Jeffreys' criterion [96] for Bayes factors. Since these injections are performed in zero noise, the Jeffreys' scale provides a conservative estimate, implying that a Bayes factor value of 0.5 could correspond to a stronger preference for the alternative hypothesis in realistic noisy scenarios.

This behavior is expected, since in the geometric optics approximation, a microlensed signal is well modeled as the superposition of two images separated by a time delay, $\tau(M_L^z, y)$.

We study this explicitly in Fig. 8, which shows the injected time difference $|\Delta t_c|$ versus the inferred lensing time delay $\tau(M_L^z, y)$ between the microlensed images (Eq. 4.5 in Ref. [47]), for a lens system with M_L^z and y corresponding to the inferred maximum-a-posteriori (MAP) values. Specifically, we compare $|\Delta t_c|$ with $T(M_L^z, y) \equiv \min\{\tau(M_L^z, y), 4 - \tau(M_L^z, y)\}$ to account for the wrap-around effect arising from the finite 4 s analysis duration used in the PE, where the delayed image can appear before the primary one within the analysis window. It is interesting to note that the inferred $T(M_L^z, y)$ values typically lie close to the corresponding $|\Delta t_c|$ values. This indicates that false evidence for microlensing signatures can arise because, to a reasonable approximation, the model produces two superimposed images whose time delay can closely match either the injected $|\Delta t_c|$ or $(\delta - |\Delta t_c|)$, where δ denotes the analysis duration ($= 4$ s) used in PE. The slight offsets between $|\Delta t_c|$ and $T(M_L^z, y)$ are expected and arise primarily due to three factors: (i) the intuition of overlapping images holds strictly in the geometrical-optics limit and may not fully capture wave-optics effects;(ii) systematic biases resulting from differences between the injection and recovery models; and (iii) inherent statistical uncertainties in the PE process.

Overall, the PE results show that both Type-II and microlensed models can provide modest improvements in fit over the unlensed model, though for different reasons in specific regions of the relative overlapping parameter space. This highlights the risk of misinterpreting overlapping events as gravitationally lensed.

B. Fitting Factor Studies

Although Bayes-factor estimates derived from fitting factors in Eq. (12) are most reliable in the high-SNR regime, and the best-fit template parameters may converge less robustly than the fitting factor itself, the approach provides a practical means to explore population-level trends. Preliminary results confirm that lower fitting factors correspond to reduced effective SNRs, which in turn degrade detection efficiency and bias parameter inference.

We extended the fitting factor study to the population of overlapping signals drawn from realistic BBH distributions sampled from astropysically motivated priors. Fig. 9 summarizes results for unlensed quasicircular templates. We have an asymmetry in the relative chirp mass biases inferred, with respect to $\mathrm{SINGLES_A}$ and $\mathrm{SINGLES_B}$, likely due to the geocentric time of the higher SNR signal ($\mathrm{SINGLES_A}$) aiding the inference. We have marginalized the representations over $\mathrm{SNR_B/SNR_A}$ and Δt_c, since the distributions are similar, with the significant parameter of interest being the chirp mass ratio $\mathscr{M}_B/\mathscr{M}_A$. Our studies align with previous works for the chirp mass biases, and we have higher biases for $\mathrm{SINGLES_B}$ at lower $\mathscr{M}_B/\mathscr{M}_A$, and
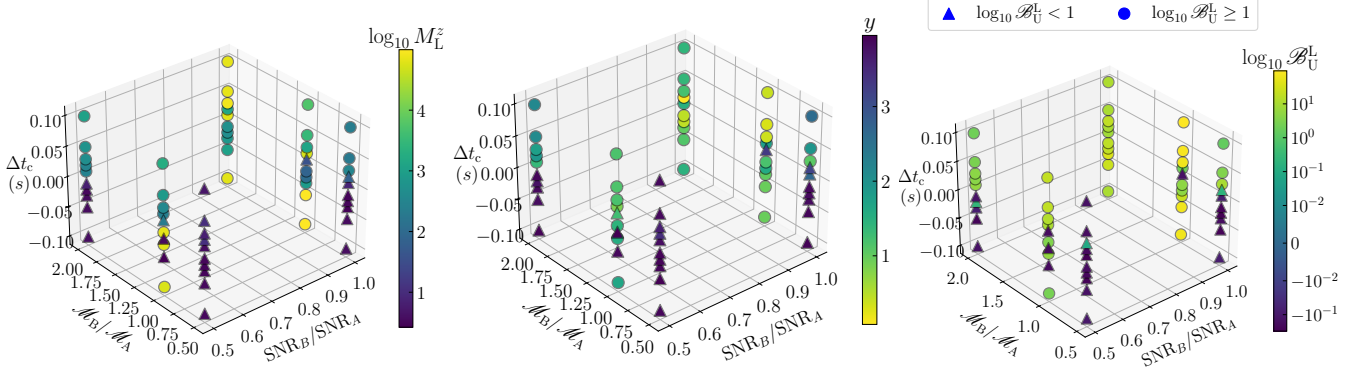
Figure 6. Inference of overlapping signals using microlensed templates for an isolated point-mass lens. *Left:* Inferred logarithmic redshifted lens mass $\log_{10} M_{\rm L}^z/{\rm M}_\odot$. *Middle:* Inferred dimensionless impact parameter y. *Right:* Bayes factor comparison between microlensed and unlensed hypotheses, with circular markers indicating $\log_{10} \mathscr{B}_{\rm U}^{\rm L} \geq 1$.
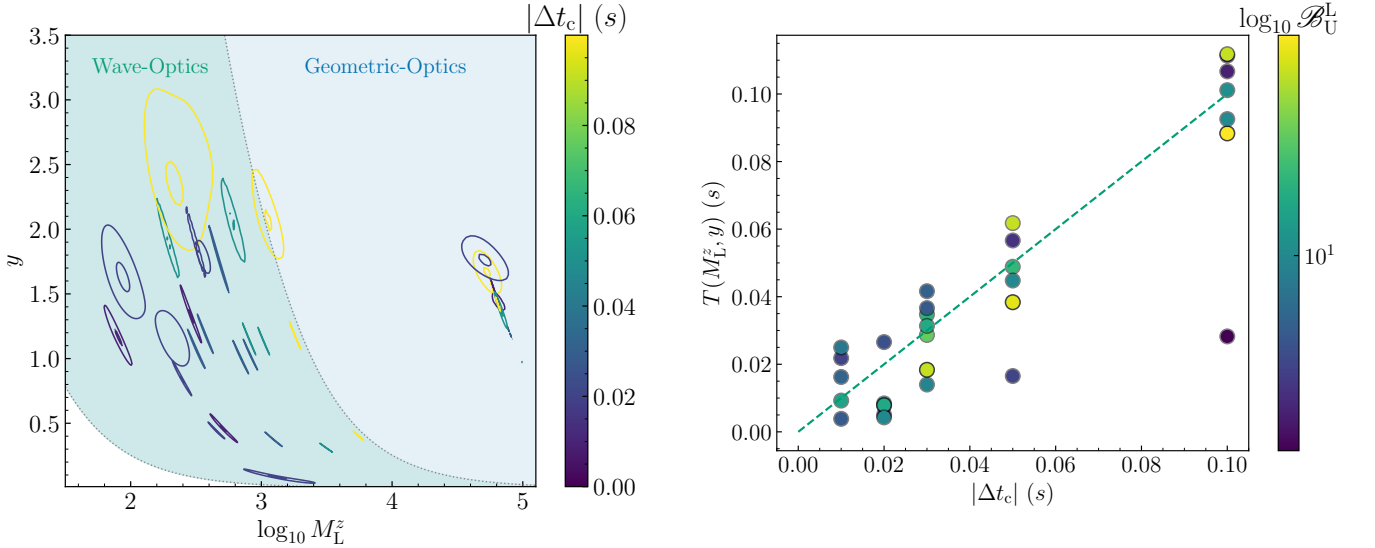

Figure 7. Joint 2D marginalized posterior distribution of the inferred logarithmic redshifted lens mass $M_{\rm L}^z$ and impact parameter y, assuming an isolated point-lens model, for the injected overlapping signals. The color scale encodes the coalescence time difference $|\Delta t_{\rm c}|$, and the level sets indicate the 50% and 95% confidence intervals. Only cases with substantial evidence in favor of microlensing ($\log_{10} \mathscr{B}_{\rm U}^{\rm L} > 0.5$) are shown for clarity. The shaded green (orange) region indicates where wave-optics (geometric-optics) effects are expected to dominate, determined by the inferred microlensing time delay between the images, $\tau(M_{\rm L}^z, y)$.

Figure 8. Comparison between the injected time difference $|\Delta t_{\rm c}|$ between the overlapping signals and the inferred lensing time delay $\tau(M_{\rm L}^z, y)$ between the microlensed images (Eq. 4.5 in Ref. [47]), for a lens system with redshifted lens mass $M_{\rm L}^z$ and impact parameter y corresponding to the inferred PE values. Specifically, we compute $T(M_{\rm L}^z, y) = \min\{\tau(M_{\rm L}^z, y),\ 4 - \tau(M_{\rm L}^z, y)\}$ to account for the wrap-around effect arising from the finite 4 s analysis duration used in PE, where the delayed image can appear before the primary one within the analysis window. The color scale represents $\log_{10} \mathscr{B}_{\rm U}^{\rm L}$, and only cases with substantial evidence for microlensing ($\log_{10} \mathscr{B}_{\rm U}^{\rm L} > 0.5$) are shown. The dashed green line indicates $|\Delta t_{\rm c}| = \tau(M_{\rm L}^z, y)$ for reference.

1. Type-II Lensed Template

Fig. 10 presents fitting factor results for the Type-II lensing hypothesis. When the Morse index is allowed to vary, the inferred index typically clusters around $n_j \simeq 0.5$ in the most overlapping scenarios. This is consistent with the PE results, suggesting a signature of Type-II Lens-
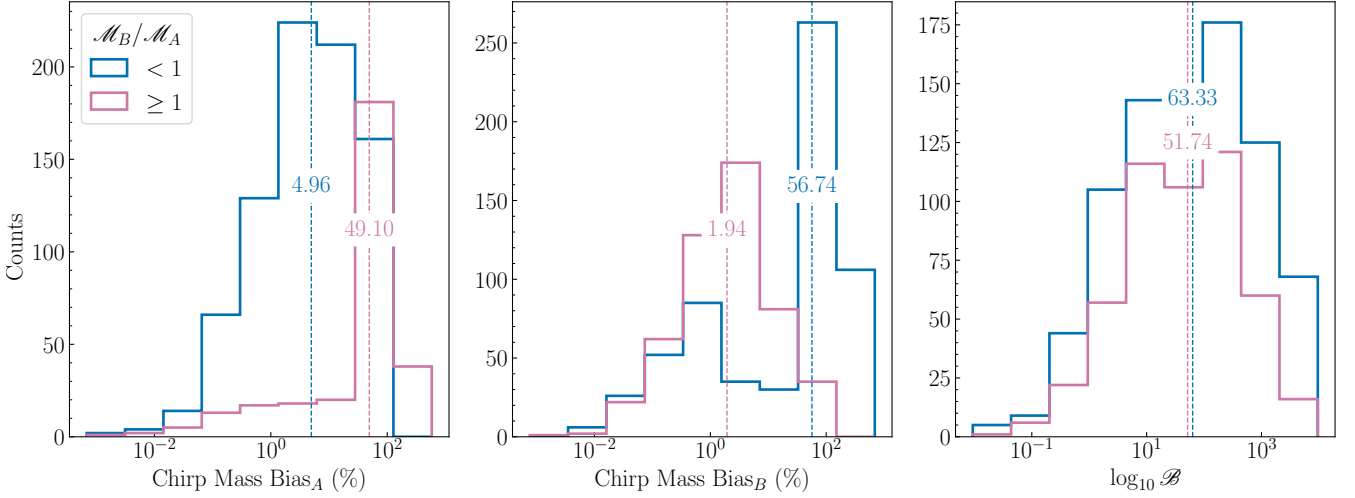
vice-versa. The Bayes factor $\log_{10} \mathscr{B}$ provides an estimate from Eq. (12), which seems to have similar distributions for smaller and larger chirp mass ratios.

Figure 9. *Left* and *Middle:* Chirp mass biases, *Right:* Bayes factors for a population of overlapping signals, obtained from fitting factor optimization with unlensed quasicircular templates. Bayes factor $\log_{10} \mathscr{B}$ quantifies the evidence in favor of an unlensed quasicircular signal over noise, estimated via Eq. (12). The histograms have been marginalized over $\mathrm{SNR_B/SNR_A}$ and Δt_c. The color represents differentiation for $\mathscr{M}_B/\mathscr{M}_A < 1$ and $\mathscr{M}_B/\mathscr{M}_A \geq 1$. Dashed lines denote the overall medians across the population.
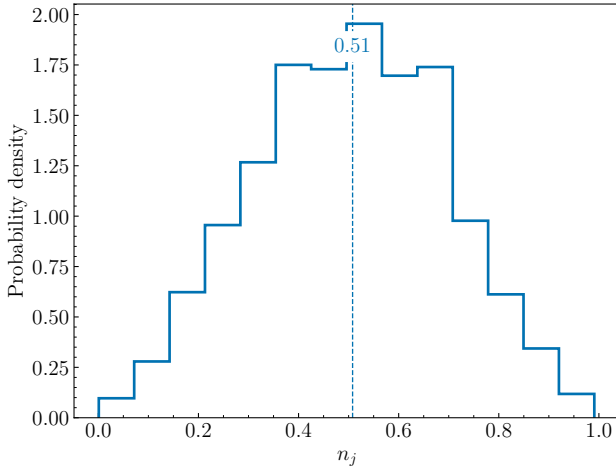

Figure 10. Population analysis of overlapping signals inferred with Type-II lensed templates. Results of the Morse phase densities when n_j is varied to maximize the match. The histogram is marginalized over the ratios $\mathscr{M}_B/\mathscr{M}_A$, $\mathrm{SNR_B/SNR_A}$ and Δt_c due to their similar distributions. Dashed lines denote the overall medians across the population.

ing. We don't observe any specific trend in the relative parameter space of the overlapping signals; hence, the histograms are marginalized over the intrinsic parameters of interest. Although not shown here, the Bayes factors estimated from the FF show a significant peak around 0, with mild support when the Morse index varies.

2. Microlensed Template

Population results for microlensed templates are shown in Fig. 11. The inference across the population has moderate lens masses, peaking in the range of 10^2–10^3 $\mathrm{M_\odot}$, and large impact parameters, $y > 2$. We observe two different peaks in the lens mass, with moderate lens masses ($\sim 10^2$ $\mathrm{M_\odot}$) being inferred by negative Δt_c, and larger values ($\sim 10^3$ $\mathrm{M_\odot}$) seen in $\Delta t_c > 0$, similar to the trends observed for the PE inferences in Sec. V A 2, specifically in Fig. 6. The Bayes factors are predominantly clustered around 0, with a subtle preference for positive Bayes factors for $\mathrm{SNR_B/SNR_A} \sim 1$, for a symmetric SNR of both signals. This suggests that lensing is likely degenerate with overlapping signals, when two signals of similar loudness interfere, which aligns with the inferences from the PE results in Sec. V A 2. The FF analysis thus confirms that the degeneracy between microlensing and overlapping signals is confined to a specific and narrow region of the parameter space, characterized by comparable SNRs. In all other regimes, the unlensed hypothesis remains the preferred explanation, with slight negative Bayes factor recoveries, especially for disparate loudness.

VI. CONCLUSIONS

With increasing sensitivity of the current and future GW detectors, the likelihood of observing two unrelated overlapping GW signals or signals that are gravitationally lensed will rise. In this work, we have investigated the potential of such overlapping signals to mimic the modulations due to gravitational lensing, focusing on two scenarios: *Type-II* strong lensing and *microlensing* in the
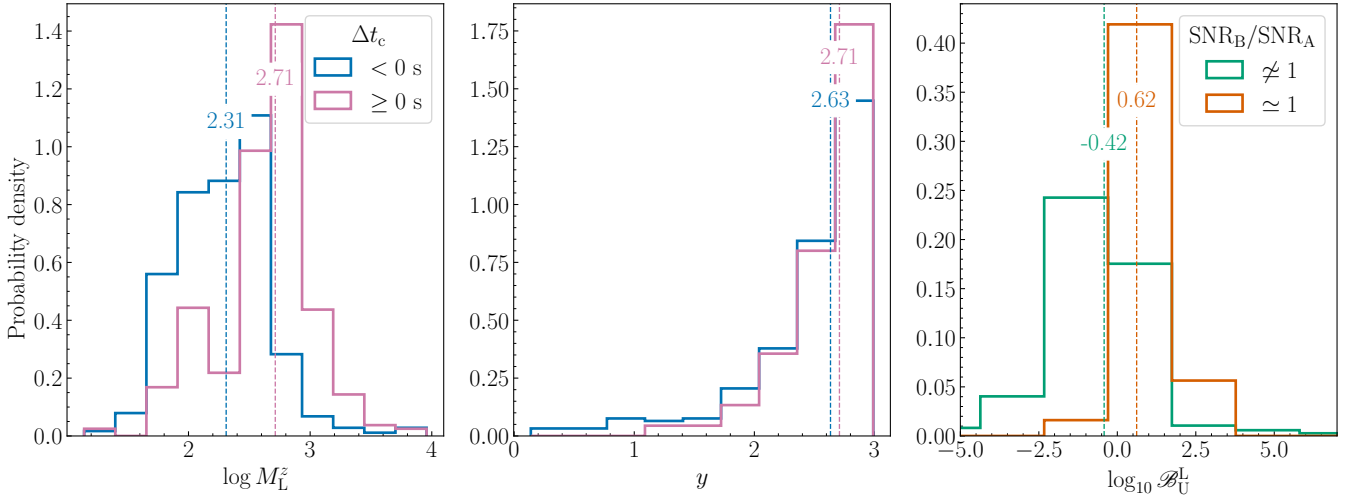
Figure 11. Fitting-factor results for overlapping signal populations using microlensed templates. *Left:* Inferred redshifted lens mass $\log_{10} M_{\mathrm{L}}^z$ densities, *Middle:* Impact parameter y densities, *Right:* Bayes factor support for microlensed model over unlensed, estimated using Eq. (12). The lens masses peak around $M_{\mathrm{L}}^z \sim 10^2 \mathrm{M}_\odot$ for negative coalescence time differences, and $M_{\mathrm{L}}^z \sim 10^3 \mathrm{M}_\odot$ for positive Δt_{c}, and we infer large impact parameters $y \sim 2.5$ for both cases. For the Bayes factor difference, the parameter space of interest was directed by the PE results in Sec. V A 2, against $\mathrm{SNR}_{\mathrm{B}}/\mathrm{SNR}_{\mathrm{A}}$, and marginalizing over $\mathscr{M}_{\mathrm{B}}/\mathscr{M}_{\mathrm{A}}$ and Δt_{c}. Dashed lines denote the overall medians across the population.

wave-optics regime.

We generated a simulated zero-noise population, each comprising two overlapping GW signals with varied chirp mass ratios $\mathscr{M}_{\mathrm{B}}/\mathscr{M}_{\mathrm{A}}$, SNR ratios $\mathrm{SNR}_{\mathrm{B}}/\mathrm{SNR}_{\mathrm{A}}$, and coalescence time differences $\Delta t_{\mathrm{c}} = t_{\mathrm{c}}^B - t_c^A$. To explore degeneracies between overlapping binaries and lensed signals, we employ two complementary approaches: (i) full Bayesian PE using `dynesty` nested sampler as implemented in `BILBY`, and (ii) fitting factor optimization to identify the best-matching template. Both methods were used for Bayesian model selection, comparing the lensed and unlensed hypotheses via the Bayes factors defined in Eqs. (8) and (12).

A targeted PE analysis was first performed on 60 injections spanning $\mathscr{M}_{\mathrm{B}}/\mathscr{M}_{\mathrm{A}} \in \{0.5, 1, 2\}$, $\mathrm{SNR}_{\mathrm{B}}/\mathrm{SNR}_{\mathrm{A}} \in \{0.5, 1\}$, and $\Delta t_{\mathrm{c}} \in [-0.1, 0.1]$ s, using lensed templates. We then extended the analysis to population studies of $\mathcal{O}(5000)$ signals, using FF optimization for computational efficiency. The main findings are:

- *Type-II Lensed (PE)*: A preference for Type-II lensing ($\log_{10} \mathscr{B}_{\mathrm{U}}^{\mathrm{L}} > 1$) arises only in a small region of parameter space, $|\Delta t_{\mathrm{c}}| \leq 0.03$ s. The median inferred Morse index is around $n_j \simeq 0.5$, consistent with the saddle-point image of Type-II lensing.

- *Type-II Lensed (FF)*: The support for the Type-II lensed hypothesis is confined to a small region of the population parameter space of interplay of $\mathscr{M}_{\mathrm{B}}/\mathscr{M}_{\mathrm{A}}$ and the $|\Delta t_{\mathrm{c}}|$, with the inferred Morse index clustered around $n_j \simeq 0.5$, and does not provide any clear trend with any of the relative parameters. The

FF results are consistent with the trends observed in the PE analyses.

- *Microlensing (PE)*: The false evidence for microlensing signatures generally arises because the model can, to a reasonable approximation, produce two superimposed images with time delay closely matching either $|\Delta t_{\mathrm{c}}|$ or $(\delta - |\Delta t_{\mathrm{c}}|)$, where δ is the analysis duration (4 s) used in PE. We infer redshifted lens masses in the range $M_{\mathrm{L}}^z \sim 10^2$–$10^5$ $\mathrm{M}_\odot$ and impact parameters $y \sim 0.1$–3. We note that as $|\Delta t_{\mathrm{c}}|$ decreases from 0.1 s to 0.01 s, the inferred $\log_{10} M_{\mathrm{L}}^z$ and y values typically decrease, from the geometric optics regime, to where wave optics effects dominate. The maximum support occurs for $\mathscr{M}_{\mathrm{B}}/\mathscr{M}_{\mathrm{A}} = \mathrm{SNR}_{\mathrm{B}}/\mathrm{SNR}_{\mathrm{A}} = 1$, and this support increases as $|\Delta t_{\mathrm{c}}|$ increases. For $\mathrm{SNR}_{\mathrm{B}}/\mathrm{SNR}_{\mathrm{A}} = 1$ and $\mathscr{M}_{\mathrm{B}}/\mathscr{M}_{\mathrm{A}} = 2$, all Δt_{c} values preferred microlensing.

- *Microlensing (FF)*: FF optimization shows moderate microlensing support when $\mathrm{SNR}_{\mathrm{B}}/\mathrm{SNR}_{\mathrm{A}} \sim 1$, consistent with PE trends. Outside this region, we have negative Bayes factors, and the unlensed model is preferred.

These results highlight that overlaps between two black hole binaries can produce biased parameter inference and false support for lensing hypotheses, particularly mimicking microlensing. False support for Type-II lensing is minimal, occurring only for very strongly overlapping cases with $|\Delta t_{\mathrm{c}}| \lesssim 0.03$ s. In contrast, false evidence for microlensing generally arises when the model produces

two images whose time delay matches either the injected $|\Delta t_{\rm c}|$ or $(\delta - |\Delta t_{\rm c}|)$. The inferred lens masses and impact parameters depend on the temporal overlap, with maximal support for equal-mass, equal-SNR binaries. These degeneracies can reduce the effective SNR, degrade detection efficiency, and increase the risk of misclassification.

In the future, the growing sensitivity of GW detectors will increase the probability of overlaps, especially for long-duration signals. Accounting for the possibility of overlapping events will therefore be essential before attributing waveform modulations to lensing. Moreover, overlap-induced waveform interference can mimic other physical effects: in particular, the modulation can be qualitatively similar to the signature of orbital eccentricity. We will address this degeneracy between overlapping and eccentric signals in our future work, aiming to disentangle these scenarios and ensure robust astrophysical interpretation of forthcoming GW detections.

ACKNOWLEDGEMENTS

DATA AVAILABILITY

The analysis codes for the PE and FF analyses of overlapping GW signals used in this work are publicly made available at the repository on Github: 🔗.

[1] J. Aasi et al. Advanced LIGO. *Class. Quant. Grav.*, 32:074001, 2015.

[2] F. Acernese et al. Advanced Virgo: a second-generation interferometric gravitational wave detector. *Class. Quant. Grav.*, 32(2):024001, 2015.

[3] R. Abbott et al. GWTC-3: Compact Binary Coalescences Observed by LIGO and Virgo during the Second Part of the Third Observing Run. *Phys. Rev. X*, 13(4):041039, 2023.

[4] GraceDB. Gracedb ligo/virgo/kagra public alerts.

[5] Kentaro Somiya. Detector configuration of KAGRA: The Japanese cryogenic gravitational-wave detector. *Class. Quant. Grav.*, 29:124007, 2012.

[6] Yoichi Aso, Yuta Michimura, Kentaro Somiya, Masaki Ando, Osamu Miyakawa, Takanori Sekiguchi, Daisuke Tatsumi, and Hiroaki Yamamoto. Interferometer design of the KAGRA gravitational wave detector. *Phys. Rev. D*, 88(4):043007, 2013.

[7] T. Akutsu et al. KAGRA: 2.5 Generation Interferometric Gravitational Wave Detector. *Nature Astron.*, 3(1):35–40, 2019.

[8] T. Akutsu et al. Overview of KAGRA: Detector design and construction history. *PTEP*, 2021(5):05A101, 2021.

[9] Bala Iyer, Tarun Souradeep, CS Unnikrishnan, Sanjeev Dhurandhar, Sandhi Raja, and Anand Sengupta. LIGO-India Tech. rep. , 2011.

[10] C. S. Unnikrishnan. IndIGO and LIGO-India: Scope and plans for gravitational wave research and precision metrology in India. *Int. J. Mod. Phys. D*, 22:1341010, 2013.

[11] P. Ajith et al. Gravitational physics in the context of Indian astronomy: A vision document. *J. Astrophys. Astron.*, 46(1):6, 2025.

[12] M. Punturo et al. The Einstein Telescope: A third-generation gravitational wave observatory. *Class. Quant. Grav.*, 27:194002, 2010.

[13] S. Hild et al. Sensitivity Studies for Third-Generation Gravitational Wave Observatories. *Class. Quant. Grav.*, 28:094013, 2011.

[14] David Reitze et al. Cosmic Explorer: The U.S. Contribution to Gravitational-Wave Astronomy beyond LIGO. *Bull. Am. Astron. Soc.*, 51(7):035, 2019.

[15] Benjamin P Abbott et al. Exploring the Sensitivity of Next Generation Gravitational Wave Detectors. *Class. Quant. Grav.*, 34(4):044001, 2017.

[16] T. Regimbau, M. Evans, N. Christensen, E. Katsavounidis, B. Sathyaprakash, and S. Vitale. Digging deeper: Observing primordial gravitational waves below the binary black hole produced stochastic background. *Phys. Rev. Lett.*, 118(15):151105, 2017.

[17] Michele Maggiore et al. Science Case for the Einstein Telescope. *JCAP*, 03:050, 2020.

[18] B. Sathyaprakash et al. Scientific Objectives of Einstein Telescope. *Class. Quant. Grav.*, 29:124013, 2012. [Erratum: Class.Quant.Grav. 30, 079501 (2013)].

[19] Marica Branchesi et al. Science with the Einstein Telescope: a comparison of different designs. *JCAP*, 07:068, 2023.

[20] Tania Regimbau and Scott A. Hughes. Gravitational-wave confusion background from cosmological compact binaries: Implications for future terrestrial detectors. *Phys. Rev. D*, 79:062002, 2009.

[21] Anuradha Samajdar, Justin Janquart, Chris Van Den Broeck, and Tim Dietrich. Biases in parameter estimation from overlapping gravitational-wave signals in the third-generation detector era. *Phys. Rev. D*, 104(4):044003, 2021.

[22] Elia Pizzati, Surabhi Sachdev, Anuradha Gupta, and Bangalore Sathyaprakash. Toward inference of overlapping gravitational-wave signals. *Phys. Rev. D*, 105(10):104016, 2022.

[23] Philip Relton and Vivien Raymond. Parameter estimation bias from overlapping binary black hole events in second generation interferometers. *Phys. Rev. D*, 104(8):084039, 2021.

[24] Andrea Antonelli, Ollie Burke, and Jonathan R. Gair. Noisy neighbours: inference biases from overlapping gravitational-wave signals. *Mon. Not. Roy. Astron. Soc.*, 507(4):5069–5086, 2021.

[25] Yoshiaki Himemoto, Atsushi Nishizawa, and Atsushi Taruya. Impacts of overlapping gravitational-wave signals on the parameter estimation: Toward the search for cosmological backgrounds. *Phys. Rev. D*, 104(4):044010, 2021.

[26] Justin Janquart, Tomasz Baka, Anuradha Samajdar, Tim Dietrich, and Chris Van Den Broeck. Analyses of overlapping gravitational wave signals using hierarchical subtraction and joint parameter estimation. *Mon. Not. Roy. Astron. Soc.*, 523(2):1699–1710, 2023.

[27] Lorenzo Speri, Nikolaos Karnesis, Arianna I. Renzini, and Jonathan R. Gair. A roadmap of gravitational wave data analysis. *Nature Astron.*, 6(12):1356–1363, 2022.

[28] Rui Niu and Wen Zhao. Extracting overlapping gravitational-wave signals of galactic compact binaries: a mini review. 6 2024.

[29] Ziming Wang, Zexin Hu, and Lijing Shao. Rigorous analytic solution to the gravitational-wave overlapping event rates. *arXiv preprint*, 1 2025.

[30] Philip Relton, Andrea Virtuoso, Sophie Bini, Vivien Raymond, Ian Harry, Marco Drago, Claudia Lazzaro, Andrea Miani, and Shubhanshu Tiwari. Addressing the challenges of detecting time-overlapping compact binary coalescences. *Phys. Rev. D*, 106(10):104045, 2022.

[31] Qian Hu and John Veitch. Accumulating Errors in Tests of General Relativity with Gravitational Waves: Overlapping Signals and Inaccurate Waveforms. *Astrophys. J.*, 945(2):103, 2023.

[32] Ziming Wang, Dicong Liang, Junjie Zhao, Chang Liu, and Lijing Shao. Anatomy of parameter-estimation biases in overlapping gravitational-wave signals. *Class. Quant. Grav.*, 41(5):055011, 2024.

[33] Jurriaan Langendorff, Alex Kolmus, Justin Janquart, and Chris Van Den Broeck. Normalizing Flows as an Avenue to Studying Overlapping Gravitational Wave Signals. *Phys. Rev. Lett.*, 130(17):171402, 2023.

[34] James Alvey, Uddipta Bhardwaj, Samaya Nissanke, and Christoph Weniger. What to do when things get crowded? Scalable joint analysis of overlapping gravitational wave signals. *arXiv preprint*, 8 2023.

[35] Yixuan Dang, Ziming Wang, Dicong Liang, and Lijing Shao. Impact of Overlapping Signals on Parameterized Post-Newtonian Coefficients in Tests of Gravity. *Astrophys. J.*, 964(2):194, 2024.

[36] Aaron D. Johnson, Katerina Chatziioannou, and Will M. Farr. Source confusion from neutron star binaries in ground-based gravitational wave detectors is minimal. *Phys. Rev. D*, 109(8):084015, 2024.

[37] Qian Hu. Hierarchical Subtraction with Neural Density Estimators as a General Solution to Overlapping Gravitational Wave Signals. 7 2025.

[38] Tomasz Baka, Harsh Narola, Justin Janquart, Anuradha Samajdar, Tim Dietrich, and Chris Van Den Broeck. Overlapping signals in next-generation gravitational wave observatories: A recipe for selecting the best parameter estimation technique. *arXiv preprint*, 7 2025.

[39] S. Klimenko et al. Method for detection and reconstruction of gravitational wave transients with networks of advanced detectors. *Phys. Rev. D*, 93(4):042004, 2016.

[40] Sergey Klimenko, Gabriele Vedovato, Valentin Necula, Francesco Salemi, Marco Drago, Eric Chassande-Mottin, Vaibhav Tiwari, Claudia Lazzaro, Brendan O'Brian, Marek Szczepanczyk, Shubhanshu Tiwari, and V. Gayathri. cwb pipeline library: 6.4.0, January 2021.

[41] Tanmaya Mishra, Shubhagata Bhaumik, V. Gayathri, Marek J. Szczepańczyk, Imre Bartos, and Sergey Klimenko. Gravitational waves detected by a burst search in LIGO/Virgo's third observing run. *Phys. Rev. D*, 111(2):023054, 2025.

[42] Anuradha Gupta et al. Possible causes of false general relativity violations in gravitational wave observations. 5 2024.

[43] B. P. Abbott et al. Properties of the Binary Black Hole Merger GW150914. *Phys. Rev. Lett.*, 116(24):241102, 2016.

[44] B. P. Abbott et al. Tests of general relativity with GW150914. *Phys. Rev. Lett.*, 116(22):221101, 2016. [Erratum: Phys.Rev.Lett. 121, 129902 (2018)].

[45] B. P. Abbott et al. GWTC-1: A Gravitational-Wave Transient Catalog of Compact Binary Mergers Observed by LIGO and Virgo during the First and Second Observing Runs. *Phys. Rev. X*, 9(3):031040, 2019.

[46] B. P. Abbott et al. GW170814: A Three-Detector Observation of Gravitational Waves from a Binary Black Hole Coalescence. *Phys. Rev. Lett.*, 119(14):141101, 2017.

[47] Takahiro T. Nakamura and Shuji Deguchi. Wave Optics in Gravitational Lensing. *Prog. Theor. Phys. Suppl.*, 133:137–153, 1999.

[48] Ryuichi Takahashi and Takashi Nakamura. Wave effects in gravitational lensing of gravitational waves from chirping binaries. *Astrophys. J.*, 595:1039–1051, 2003.

[49] Liang Dai and Tejaswi Venumadhav. On the waveforms of gravitationally lensed gravitational waves. *arXiv preprint*, 2 2017.

[50] Jose María Ezquiaga, Daniel E. Holz, Wayne Hu, Macarena Lagos, and Robert M. Wald. Phase effects from strong gravitational lensing of gravitational waves. *Phys. Rev. D*, 103(6):064047, 2021.

[51] Aditya Vijaykumar, Ajit Kumar Mehta, and Apratim Ganguly. Detection and parameter estimation challenges of type-II lensed binary black hole signals. *Phys. Rev. D*, 108(4):043036, 2023.

[52] Mick Wright, Justin Janquart, and Nathan K. Johnson-McDaniel. Effect of Deviations from General Relativity on Searches for Gravitational Wave Microlensing and Type II Strong Lensing. *arXiv preprint*, 3 2024.

[53] S. Basak, A. Ganguly, K. Haris, S. Kapadia, A. K. Mehta, and P. Ajith. Constraints on Compact Dark Matter from Gravitational Wave Microlensing. *Astrophys. J.*, 926(2):L28, 2022.

[54] Anuj Mishra, Ashish Kumar Meena, Anupreeta More, and Sukanta Bose. Exploring the impact of microlensing on gravitational wave signals: Biases, population characteristics, and prospects for detection. *Mon. Not. Roy. Astron. Soc.*, 531(1):764–787, 2024.

[55] Peter Schneider, Jürgen Ehlers, and Emilio E. Falco. *Gravitational Lenses*. Astronomy and Astrophysics Library. Springer, 1992.

[56] Justin Janquart et al. Follow-up analyses to the O3 LIGO–Virgo–KAGRA lensing searches. *Mon. Not. Roy. Astron. Soc.*, 526(3):3832–3860, 2023.

[57] Ashish Kumar Meena and J. S. Bagla. Gravitational lensing of gravitational waves: wave nature and prospects for detection. *Mon. Not. Roy. Astron. Soc.*, 492(1):1127–1134, 2020.

[58] Anuj Mishra, Ashish Kumar Meena, Anupreeta More, Sukanta Bose, and Jasjeet Singh Bagla. Gravitational lensing of gravitational waves: effect of microlens population in lensing galaxies. *Mon. Not. Roy. Astron. Soc.*, 508(4):4869–4886, 2021.

[59] R. Abbott et al. Search for Gravitational-lensing Signatures in the Full Third Observing Run of the LIGO–Virgo Network. *Astrophys. J.*, 970(2):191, 2024.

[60] Anuj Mishra, N. V. Krishnendu, and Apratim Ganguly. Unveiling microlensing biases in testing general relativity with gravitational waves. *Phys. Rev. D*, 110(8):084009, 2024.

[61] Anna Liu, Isaac C. F. Wong, Samson H. W. Leong, Anupreeta More, Otto A. Hannuksela, and Tjonnie G. F. Li. Exploring the hidden Universe: a novel phenomenological approach for recovering arbitrary gravitational-wave millilensing configurations. *Mon. Not. Roy. Astron. Soc.*, 525(3):4149–4160, 2023.

[62] Aniruddha Chakraborty and Suvodip Mukherjee. The First Model-independent Chromatic Microlensing Search: No Evidence in the Gravitational Wave Catalog of LIGO–Virgo–KAGRA. *Astrophys. J.*, 990(1):68, 2025.

[63] Benjamin P Abbott, R Abbott, TD Abbott, S Abraham, F Acernese, K Ackley, C Adams, VB Adya, C Affeldt, M Agathos, et al. Prospects for observing and localizing gravitational-wave transients with advanced ligo, advanced virgo and kagra. *Living reviews in relativity*, 23:1–69, 2020.

[64] R. Abbott et al. GWTC-3: Compact Binary Coalescences Observed by LIGO and Virgo During the Second Part of the Third Observing Run. 11 2021.

[65] Maya Fishbach, Daniel E. Holz, and Will M. Farr. Does the Black Hole Merger Rate Evolve with Redshift? *Astrophys. J. Lett.*, 863(2):L41, 2018.

[66] Daniel Wysocki, Jacob Lange, and Richard O'Shaughnessy.

Reconstructing phenomenological distributions of compact binaries via gravitational wave observations. *Phys. Rev. D*, 100(4):043012, 2019.

[67] Benjamin J. Owen. Search templates for gravitational waves from inspiraling binaries: Choice of template spacing. *Phys. Rev. D*, 53:6749–6761, 1996.

[68] Benjamin J. Owen and B. S. Sathyaprakash. Matched filtering of gravitational waves from inspiraling compact binaries: Computational cost and template placement. *Phys. Rev. D*, 60:022002, 1999.

[69] Jeffrey C. Lagarias, James A. Reeds, Margaret H. Wright, and Paul E. Wright. Convergence Properties of the Nelder-Mead Simplex Method in Low Dimensions. *SIAM J. Optim.*, 9:112–147, 1998.

[70] Piotr Jaranowski and Andrzej Krolak. Gravitational-Wave Data Analysis. Formalism and Sample Applications: The Gaussian Case. *Living Rev. Rel.*, 8:3, 2005.

[71] P. Ajith et al. A Template bank for gravitational waveforms from coalescing binary black holes. I. Non-spinning binaries. *Phys. Rev. D*, 77:104017, 2008. [Erratum: Phys.Rev.D 79, 129901 (2009)].

[72] P. Ajith. Gravitational-wave data analysis using binary black-hole waveforms. *Class. Quant. Grav.*, 25:114033, 2008.

[73] Juan Calderón Bustillo, Sascha Husa, Alicia M. Sintes, and Michael Pürrer. Impact of gravitational radiation higher order modes on single aligned-spin gravitational wave searches for binary black holes. *Phys. Rev. D*, 93(8):084019, 2016.

[74] P. Ajith, N. Fotopoulos, S. Privitera, A. Neunzert, and A. J. Weinstein. Effectual template bank for the detection of gravitational waves from inspiralling compact binaries with generic spins. *Phys. Rev. D*, 89(8):084041, 2014.

[75] Samantha A. Usman et al. The PyCBC search for gravitational waves from compact binary coalescence. *Class. Quant. Grav.*, 33(21):215004, 2016.

[76] Neil Cornish, Laura Sampson, Nicolas Yunes, and Frans Pretorius. Gravitational Wave Tests of General Relativity with the Parameterized Post-Einsteinian Framework. *Phys. Rev. D*, 84:062003, 2011.

[77] Adriano Azevedo-Filho and Ross D. Shachter. Laplace's method approximations for probabilistic inference in belief networks with continuous variables. *arXiv preprint*, 2013.

[78] Laura Sampson, Nicolas Yunes, and Neil Cornish. Rosetta stone for parametrized tests of gravity. *Phys. Rev. D*, 88(6):064056, 2013. [Erratum: Phys.Rev.D 88, 089902 (2013)].

[79] Han Gil Choi, Tao Yang, and Hyung Mok Lee. Importance of eccentricities in parameter estimation of compact binary inspirals with decihertz gravitational-wave detectors. *Phys. Rev. D*, 110(2):024025, 2024.

[80] Mark Hannam, Patricia Schmidt, Alejandro Bohé, Leïla Haegel, Sascha Husa, Frank Ohme, Geraint Pratten, and Michael Pürrer. Simple Model of Complete Precessing Black-Hole-Binary Gravitational Waveforms. *Phys. Rev. Lett.*, 113(15):151101, 2014.

[81] Sascha Husa, Sebastian Khan, Mark Hannam, Michael Pürrer, Frank Ohme, Xisco Jiménez Forteza, and Alejandro Bohé. Frequency-domain gravitational waves from nonprecessing black-hole binaries. I. New numerical waveforms and anatomy of the signal. *Phys. Rev. D*, 93(4):044006, 2016.

[82] Sebastian Khan, Sascha Husa, Mark Hannam, Frank Ohme, Michael Pürrer, Xisco Jiménez Forteza, and Alejandro Bohé. Frequency-domain gravitational waves from nonprecessing black-hole binaries. II. A phenomenological model for the advanced detector era. *Phys. Rev. D*, 93(4):044007, 2016.

[83] Geraint Pratten et al. Computationally efficient models for the dominant and subdominant harmonic modes of precessing binary black holes. *Phys. Rev. D*, 103(10):104056, 2021.

[84] Antoni Ramos-Buades, Alessandra Buonanno, Héctor Estellés, Mohammed Khalil, Deyan P. Mihaylov, Serguei Ossokine, Lorenzo Pompili, and Mahlet Shiferaw. Next generation of accurate and efficient multipolar precessing-spin effective-one-body waveforms for binary black holes. *Phys. Rev. D*, 108(12):124037, 2023.

[85] LIGO Scientific Collaboration, Virgo Collaboration, and KAGRA Collaboration. LVK Algorithm Library - LALSuite. Free software (GPL), 2018.

[86] Karl Wette. SWIGLAL: Python and Octave interfaces to the LALSuite gravitational-wave data analysis libraries. *SoftwareX*, 12:100634, 2020.

[87] Gareth S. Davies, Thomas Dent, Márton Tápai, Ian Harry, Connor McIsaac, and Alexander H. Nitz. Extending the PyCBC search for gravitational waves from compact binary mergers to a global network. *Phys. Rev. D*, 102(2):022004, 2020.

[88] Colm Talbot, Rory Smith, Eric Thrane, and Gregory B. Poole. Parallelized Inference for Gravitational-Wave Astronomy. *Phys. Rev. D*, 100(4):043030, 2019.

[89] Gregory Ashton et al. BILBY: A user-friendly Bayesian inference library for gravitational-wave astronomy. *Astrophys. J. Suppl.*, 241(2):27, 2019.

[90] Rory J. E. Smith, Gregory Ashton, Avi Vajpeyi, and Colm Talbot. Massively parallel Bayesian inference for transient gravitational-wave astronomy. *Mon. Not. Roy. Astron. Soc.*, 498(3):4492–4502, 2020.

[91] I. M. Romero-Shaw et al. Bayesian inference for compact binary coalescences with bilby: validation and application to the first LIGO–Virgo gravitational-wave transient catalogue. *Mon. Not. Roy. Astron. Soc.*, 499(3):3295–3319, 2020.

[92] Joshua S. Speagle. dynesty: a dynamic nested sampling package for estimating Bayesian posteriors and evidences. *Mon. Not. Roy. Astron. Soc.*, 493(3):3132–3158, 2020.

[93] Alex Nitz, Ian Harry, Duncan Brown, Christopher M. Biwer, Josh Willis, Tito Dal Canton, Collin Capano, Thomas Dent, Larne Pekowsky, Gareth S Cabourn Davies, Soumi De, Miriam Cabero, Shichao Wu, Andrew R. Williamson, Bernd Machenschalk, Duncan Macleod, Francesco Pannarale, Prayush Kumar, Steven Reyes, dfinstad, Sumit Kumar, Márton Tápai, Leo Singer, Praveen Kumar, veronica villa, maxtrevor, Bhooshan Uday Varsha Gadre, Sebastian Khan, Stephen Fairhurst, and Arthur Tolley. gwastro/pycbc: v2.3.3 release of pycbc, January 2024.

[94] Rainer Storn and Kenneth Price. Differential Evolution – A Simple and Efficient Heuristic for global Optimization over Continuous Spaces. *J. Global Optim.*, 11(4):341–359, 1997.

[95] Pauli Virtanen et al. SciPy 1.0–Fundamental Algorithms for Scientific Computing in Python. *Nature Meth.*, 17:261, 2020.

[96] Harold Jeffreys. *The Theory of Probability*. Oxford Classic Texts in the Physical Sciences. 1939.

[97] Robert E. Kass and Adrian E. Raftery. Bayes Factors. *J. Am. Statist. Assoc.*, 90(430):773–795, 1995.

[98] Eric Thrane and Colm Talbot. An introduction to Bayesian inference in gravitational-wave astronomy: parameter estimation, model selection, and hierarchical models. *Publ. Astron. Soc. Austral.*, 36:e010, 2019. [Erratum: Publ.Astron.Soc.Austral. 37, e036 (2020)].

[99] Walter Del Pozzo, John Veitch, and Alberto Vecchio. Testing General Relativity using Bayesian model selection: Applications to observations of gravitational waves from compact binary systems. *Phys. Rev. D*, 83:082002, 2011.